Journal of Biomedical Optics

BiomedicalOptics.SPIEDigitalLibrary.org

# Validation of quantitative attenuation and backscattering coefficient measurements by optical coherence tomography in the concentration-dependent and multiple scattering regime

Mitra Almasian
Nienke Bosschaart
Ton G. van Leeuwen
Dirk J. Faber

SPIE.

Journal of Biomedical Optics 20(12), 121314 (December 2015)

# Validation of quantitative attenuation and backscattering coefficient measurements by optical coherence tomography in the concentration-dependent and multiple scattering regime

**Mitra Almasian,[a] Nienke Bosschaart,[b] Ton G. van Leeuwen,[a] and Dirk J. Faber[a,*]**
[a]University of Amsterdam, Academic Medical Center, Department of Biomedical Engineering and Physics, Meibergdreef 9, 1105 AZ, Amsterdam, The Netherlands
[b]University of Twente, MIRA Institute for Biomedical Technology and Technical Medicine, Biomedical Photonic Imaging Group, Zuidhorst ZH263, 7500 AE, Enschede, The Netherlands

**Abstract.** Optical coherence tomography (OCT) has the potential to quantitatively measure optical properties of tissue such as the attenuation coefficient and backscattering coefficient. However, to obtain reliable values for strong scattering tissues, accurate consideration of the effects of multiple scattering and the nonlinear relation between the scattering coefficient and scatterer concentration (concentration-dependent scattering) is required. We present a comprehensive model for the OCT signal in which we quantitatively account for both effects, as well as our system parameters (confocal point spread function and sensitivity roll-off). We verify our model with experimental data from controlled phantoms of monodisperse silica beads (scattering coefficients between 1 and 30 $\mathrm{mm}^{-1}$ and scattering anisotropy between 0.4 and 0.9). The optical properties of the phantoms are calculated using Mie theory combined with the Percus–Yevick structure factor to account for concentration-dependent scattering. We demonstrate excellent agreement between the OCT attenuation and backscattering coefficient predicted by our model and experimentally derived values. We conclude that this model enables us to accurately model OCT-derived parameters (i.e., attenuation and backscattering coefficients) in the concentration-dependent and multiple scattering regime for spherical monodisperse samples. [DOI: 10.1117/1.JBO.20.12.121314]

Keywords: optical coherence tomography; concentration-dependent scattering; multiple scattering; attenuation coefficient; backscattering coefficient.

Paper 150442SSR received Jun. 30, 2015; accepted for publication Nov. 30, 2015; published online Dec. 29, 2015.

## 1 Introduction

Optical coherence tomography (OCT) is a light scattering-based imaging modality which allows micrometer-scale resolution volumetric imaging and characterization of tissue morphology. Several (preclinical) studies show a correlation between the pathological state of the tissue and an OCT-derived attenuation coefficient, $\mu_{\mathrm{OCT}}$, which quantifies the decay of the OCT signal in depth.[1–4] Despite promising results, the underlying cause of this correlation is not theoretically explained. The hypothesis of a higher attenuation for cancerous versus noncancerous[5] (relying on assumed structural differences between cancerous and noncancerous) does not seem to hold for all tissue types.[6–8] For reliable clinical use, the validation of quantitative measurement of OCT-derived attenuation coefficient ($\mu_{\mathrm{OCT}}$) and amplitude [determined by the backscattering coefficient within the numerical aperture (NA) of the optics, $\mu_{B,\mathrm{NA}}$] is paramount, e.g., to determine cut-off values for various tissue types. To obtain tissue optical properties $\mu_{\mathrm{OCT}}$ and $\mu_{B,\mathrm{NA}}$, system parameters [confocal point spread function (PSF) and sensitivity roll-off] should be calibrated for. Moreover, within the scattering regime of biological tissue effects as the concentration-dependent scattering and multiple scattering should be taken into account in order to understand the measured attenuation. Due to concentration-dependent scattering, the "bulk" scattering properties at high volume fractions cannot be calculated from super positioned scattered intensities of individual particles. Rather, scattered fields need to be added and their interference should be accounted for by incorporating a "structure factor" in the calculation of the scattering properties. The structure factor for discrete random media (DRM, i.e., suspensions of monodisperse silica beads) considered in this paper can be calculated using the Percus–Yevick equation. [9,10] Using Mie solutions to the Maxwell equations, one can calculate the scattering properties of a single spherical particle. At times, the Mie solutions for a single particle are linearly extrapolated to obtain the scattering properties of an ensemble of particles. For very dilute solutions, $\mu_S$ scales linearly with volume fraction. However, at higher concentrations, dependent scattering leads to lower values for the scattering coefficient ($\mu_S$). At higher scattering coefficients and scattering anisotropy, the contribution of multiple scattered light to the OCT signal is increased, which leads to a decreased measured $\mu_{\mathrm{OCT}}$ compared with the $\mu_S$. The separation of the effects of concentration dependent and multiple scattering is challenging, as both lower the value of $\mu_{\mathrm{OCT}}$ compared with

---

*Address all correspondence to: Dirk J. Faber, E-mail: d.j.faber@amc.uva.nl

1083-3668/2015/$25.00 © 2015 SPIE

predictions based on the linear extrapolation of Mie calculated scattering cross sections.

The aim of this study is to quantitatively derive and validate the values of $\mu_{\mathrm{OCT}}$ and $\mu_{B,\mathrm{NA}}$ from the OCT signal by correcting for system parameters and taking into account the effects of multiple and concentration-dependent scattering.

We first describe a generic model of the OCT signal in Sec. 2 in terms of system parameters (confocal PSF and sensitivity roll-off) and pursued properties $\mu_{\mathrm{OCT}}$ and $\mu_{B,\mathrm{NA}}$. We discuss the calculation of the scattering properties of the phantom materials taking into account concentration-dependent scattering. Next, we summarize the extended Huygens–Fresnel (EHF) model[11,12] to account for multiple scattering in OCT signals and combine it with the calculations of the DRM scattering properties to arrive at theoretical predictions for $\mu_{\mathrm{OCT}}$ and $\mu_{B,\mathrm{NA}}$. Section 3 describes a practical way to account for system-induced attenuation, sample preparation, and data analysis. We propose to use DRM as validation phantoms, i.e., samples of spherical scatterers with known size distribution, for which the OCT-derived $\mu_{\mathrm{OCT}}$ and $\mu_{B,\mathrm{NA}}$ can be calculated. The values of $\mu_{\mathrm{OCT}}$ and $\mu_{B,\mathrm{NA}}$ of the DRM should match the range of values found in tissue as closely as possible (roughly 1 to 30 $\mathrm{mm}^{-1}$ in our experiments). Therefore, samples of different size distributions and volume fractions need to be prepared. Finally, in Secs. 4 and 5, respectively, we present our results showing excellent agreement between experimental and predicted $\mu_{\mathrm{OCT}}$ and $\mu_{B,\mathrm{NA}}$ and discuss our results and their clinical implications.

## 2 Theory

### 2.1 *Generic Model of the Optical Coherence Tomography Signal*

The most common approach to date to quantify optical properties from OCT images is by the means of nonlinear least squares (NLLS) curve-fitting of an OCT signal model to the measured data. If the signal model is parameterized properly, such that no mutual dependence exists between the fit parameters, the covariance matrix obtained from the NLLS fit procedure yields uncertainty estimates on the fitted parameters such as standard deviation of multiple fits for which the region of interest (ROI) is changed by 10%. We adopt the model by Xu et al.,[13] which assumes only single backscattered light contributes to the OCT signal. Light to and from the backscatter location at depth $z$ is attenuated due to scattering and absorption. This is accounted for by the attenuation coefficient $\mu_t$, such that $\mu_t \mathrm{d}z$ is the probability of interaction in path length $\mathrm{d}z$ and $1-\mu_t \mathrm{d}z$ is the transmission probability. The intensity incident at the backscattering site is thus reduced by a factor $(1-\mu_t \mathrm{d}z_1)\times(1-\mu_t \mathrm{d}z_2)\times\ldots\times(1-\mu_t \mathrm{d}z_N)$ compared with the intensity impinged on the tissue. If the sample is homogeneous and the product $\mu_t \mathrm{d}z$ is small, we write $\lim_{n\to\infty}[1-\mu_t(z/n)]^n = \mathrm{e}^{-\mu_t z}$. Several preclinical and phantom studies demonstrated that, for most tissues, the OCT signal amplitude versus depth $z$ is best described by this single exponential decay curve, combined with descriptions for the confocal PSF[14,15] and sensitivity roll-off in depth for frequency domain OCT systems. The resulting expression for the mean-squared OCT depth signal after noise subtraction for $z \geq z_0$ is[16,17]

$$\langle A^2(z)\rangle = \alpha\cdot T(z-z_f)\cdot H(z) \cdot \mu_{B,\mathrm{NA}}\,\exp[-2\mu_{\mathrm{OCT}}(z-z_0)], \tag{1}$$

where $z_f$ and $z_0$ are the depth positions of the focus and the tissue boundary with respect to zero-delay, respectively, and $\alpha$ is a system-dependent factor (which can be calibrated) that includes the power incident on the sample, the quantum efficiency of the detector, and the source coherence length.[18,19] The function $T(z-z_f)$ is the confocal PSF:

$$T(z-z_f) = \frac{1}{\left(\frac{z-z_f}{2nZ_{R0}}\right)^2+1}, \tag{2}$$

where $Z_{R0}=\pi w_0^2/\lambda_0$ is the Rayleigh length (half the depth-of-focus) of the sample arm optics measured in air, and $n$ is the refractive index of the medium, $\lambda_0$ is the center wavelength of the OCT source, and $w_0$ is the beam waist at the focus (defined as the beam radius where the intensity drops to a factor $1/e^2$ of its maximum). The factor 2 accounts for the apparent doubling of the Rayleigh length for diffuse reflection.[15,20] The PSF can be calibrated, for example, by measuring the depth-of-focus using a mirror or by knife-edge measurements of $w_0$.

The expression for the sensitivity roll-off in depth $H(z)$ is given in terms of sampling and optical resolution (in wavenumbers) in the following equation:[21]

$$H(z) = \left[\frac{\sin(0.5\Delta k_{\mathrm{sampling}}z)}{0.5\Delta k_{\mathrm{sampling}}z}\right]^2 \exp\left(-\frac{\Delta k_{\mathrm{optical}}^2 z^2}{8\ln 2}\right). \tag{3}$$

The sampling resolution is calculated as $(k_{\max}-k_{\min})/N_{\mathrm{SAMP}}$, where $N_{\mathrm{SAMP}}$ is the number of pixels/samples taken per spectrum and $k_{\max}$ and $k_{\min}$ are the maximum and minimum wavenumbers supported by the spectrometer or swept source. For spectrometer-OCT systems, $\Delta k_{\mathrm{optical}}$ is determined by the dispersion line width of the spectrometer. For swept-source OCT systems, it is the instantaneous line width of the source. Both systems' resolutions, the first- and second-term in Eq. (3), can be calibrated separately. In Sec. 3.1, we present a practical approach to calibrate $T(z-z_f)$ and $H(z)$ together from an OCT measurement of very weakly scattering media.

The last term of Eq. (1), $\mu_{B,\mathrm{NA}}\,\exp[-2\mu_{\mathrm{OCT}}(z-z_0)]$, contains the optical properties of the sample, but is influenced by system properties as well. The backscattering coefficient within the NA ($\mu_{B,\mathrm{NA}}$) clearly depends on the confocal properties of the OCT system. Throughout this paper, we assume $\mu_{B,\mathrm{NA}}$ only differs per sample, but is constant in depth for homogeneous phantoms for each individual sample. The decay constant $\mu_{\mathrm{OCT}}$ depends on the scattering coefficient $\mu_S$ and absorption coefficient $\mu_A$. For weakly scattering samples, with negligible contributions from multiple scattered light, $\mu_{\mathrm{OCT}}=\mu_S+\mu_A$. The experimentally obtained value may be influenced by the contribution of multiple scattering to the OCT signal, determined by the confocal properties of the system and on the angular scattering characteristics of the sample. Both a lower NA and samples with highly forward directed scattering combined with a high scattering coefficient, corresponding to values of the scattering anisotropy $g$ close to unity, lead to larger contributions of multiple scattered light in the detected signals.[12] Thus, for these situations, detection of multiple scattered light leads to a decreased decay of the OCT signal in depth, i.e., $\mu_{\mathrm{OCT}}<\mu_S+\mu_A$. In that case, the following equation is applicable:

$$\mu_{\mathrm{OCT}} = f_{\mathrm{NA},g}(\mu_S)+\mu_A, \tag{4}$$

where the mapping function $f_{\mathrm{NA},g}$ depends on confocal system properties and sample angular scattering properties. A similar equation was proposed by Jacques et al.[22] based on Monte Carlo simulations. The calculation of $\mu_S$ and $\mu_{B,\mathrm{NA}}$ is detailed in Sec. 2.2. The multiple scattering mapping function $f_{\mathrm{NA},g}$ is discussed in Sec. 2.3. At the clinically applied wavelength of 1300 nm, scattering dominates over absorption ($\mu_S \gg \mu_A$).

## 2.2 *Optical Properties of the Phantom*

Consider an isotropic DRM consisting of identical hard spherical particles with known number density $\rho$ [# particles/m$^3$]. The particles cannot overlap in volume. For the individual particles, Mie theory[23] yields the differential scattering cross section $\sigma_S(\theta)$ (m$^{-2}$ sr$^{-1}$), where $\theta$ is the scattering angle. The total scattering cross section is found by integrating over the angular coordinates while taking into account the phase differences in the scattered fields from the different particles (which are determined by their distinct positions $r$)

$$\sigma_S = 2\pi \int_0^{\pi} \sigma_S(\theta) \left\langle \sum_{u=1}^{N} \sum_{v=1}^{N} e^{i\vec{q}(\theta)\cdot\vec{r}_u} e^{-i\vec{q}(\theta)\cdot\vec{r}_v} \right\rangle \sin\theta \, d\theta. \tag{5}$$

The term between chevrons $\langle \dots \rangle$ defines the structure factor $S(\vec{q})$, where $\vec{q}$ is the scattering vector $\vec{q} = \vec{k}_{\mathrm{out}} - \vec{k}_{\mathrm{in}}$, $|\vec{q}| = q = 2k \sin(\theta/2)$. The ensemble average runs over a volume containing $N$ particles with position $\vec{r}_u$ (and $\vec{r}_v$) and thus depends on volume fraction $f_v$. The structure factor describes the accumulative effect of interference between the fields scattered from the $N$ contributing particles under the assumption that each of the particles is illuminated by the same incident field (first Born approximation). If no interference takes place, the terms where $u \neq v$ vanish and $S = 1$. In general, interference takes place and the structure factor depends on number density $\rho$, or volume fraction $f_v = \rho V_P$ ("concentration-dependent scattering"), where $V_P = \pi D^3/6$ is the volume of a spherical particle with diameter $D$. For the DRM under consideration, the structure factor is calculated as the Fourier transform of the Percus–Yevick equation for the pair correlation function (PCF, which is interpreted as a normalized distribution of distances $r$ between particle pairs).[9,24] For dilute suspensions of hard spheres of diameter $D$, $\mathrm{PCF}(f_V, r) = 0$ when $r < D$ and unity otherwise. For higher volume fractions, $\mathrm{PCF}(f_V, r)$ shows a damped oscillatory behavior, with increased probability of finding pair separations at multiples of $D$ and decreased probability in between. In the limit $r \to \infty$, $\mathrm{PCF}(f_V, r)$ goes to unity. The structure factor that can be described as $S(f_V, \theta)$ is approximately constant at unity for low volume fractions. Equation (5) shows that nonunity $S(f_V, \theta)$ at higher values of $f_v$ causes an angular redistribution of scattered light by the medium compared with that of a single particle (it serves as a weighting function for the differential scattering cross section). Figure 1 shows a graph of the structure factor at volume fractions 0.001, 0.2, and 0.5 as function of $Dq = (kD) * 2 \sin(\theta/2)$. The curve was calculated using the algorithm described in Ref. 24, as the numerical Fourier transform of the Percus–Yevick PCF.

The scattering coefficient (the product of particle density and scattering cross section, $\mu_S = \rho\sigma_S$) is then calculated as

$$\mu_S = \frac{f_V}{V_p} \cdot 2\pi \int_0^{\pi} \sigma_S(\theta) S(f_V, \theta) \sin\theta \, d\theta. \tag{6}$$

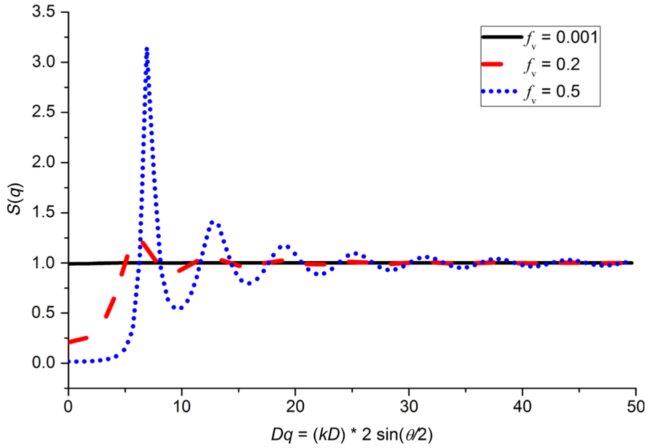

**Fig. 1** A graph of the structure factor at volume fractions $f_v = 0.001$, 0.2, and 0.5 as a function of $Dq = (kD) * 2\sin(\theta/2)$. The curve was calculated using the algorithm described by Tsang et al.,[24] as the numerical Fourier transform of the Percus–Yevick pair correlation function (PCF).

The backscattering coefficient within the detection NA is calculated similarly by adjusting the integration boundaries to $[\pi - \arcsin(\mathrm{NA})\ to\ \pi]$:

$$\mu_{B,\mathrm{NA}} = \frac{f_V}{V_p} \cdot 2\pi \int_{\pi - \arcsin(\mathrm{NA})}^{\pi} \sigma_S(\theta) S(f_V, \theta) \sin\theta \, d\theta. \tag{7}$$

Consequently, both $\mu_{\mathrm{OCT}}$ and $\mu_{B,\mathrm{NA}}$ depend both on the differential scattering cross section of the particles comprising the DRM (calculated by Mie theory) and on the volume fraction of the particles (accounted for by the Percus–Yevick structure factor).

## 2.3 *Multiple Scattering Model*

For a high value of the sample's scattering coefficient ($\mu_S$) and a scattering anisotropy ($g$) close to 1, an increased contribution of multiple scattered light to the OCT signal will lead to a reduced measured $\mu_{\mathrm{OCT}}$. The most comprehensive model to date describing this effect is based on the EHF principle introduced by Schmitt and Knüttel[11] and Thrane et al.[12] Here, in the paraxial approximation, the mean squared OCT signal—excluding the effects on attenuation of the confocal PSF and sensitivity roll-off—is given by a contribution of three terms: the single-backscattered field [as in Eq. (1)], the multiple (forward) scattered field, and a coherent cross term between these two fields as

$$\langle A^2(z) \rangle \propto \exp(-2\mu_S z) + \frac{2\exp(-\mu_S z)[1 - \exp(-\mu_S z)]}{1 + \frac{w_S^2(z)}{w_H^2(z)}} + [1 - \exp(-\mu_S z)]^2 \frac{w_H^2(z)}{w_S^2(z)}. \tag{8}$$

To maintain readability of the equations, we substituted $\Delta z = z - z_0$ in the equations in this paragraph, so that $\Delta z$ should be interpreted as the depth coordinate in tissue measured from the sample boundary at $Z_0$.

Here, $w_H(z)$ is the local beam waist in the absence of forward scattering (e.g., of the single-backscattered beam):

$$w_H^2(\Delta z) = w_0^2 \left[ \left( \frac{z - z_f}{2nZ_{RO}} \right)^2 + 1 \right], \tag{9}$$

where $w_0$ is the beam waist at the focus, measured in air as before (Sec. 2.1). The factor 2 in the denominator of the term between square brackets $[\dots]$ accounts for the apparent doubling of the Rayleigh length for diffuse reflection.[15,20] The expression for the local beam waist in the presence of multiple forward scattering $w_S(z)$ can be found in Ref. 12 as

$$w_S^2(\Delta z) = w_H^2(\Delta z) + \frac{1}{3}(\mu_S \Delta z)\theta_{\mathrm{rms}}^2(\Delta z/n). \tag{10}$$

The broadening of the beam thus depends on the average number of scattering events $\mu_S z$ and on the angular distribution of the scattered light. In the EHF model, this distribution is described through the root-mean-square (rms) scattering angle $\theta_{\mathrm{rms}}$ (a small value for small scattering angles; compared with the scattering anisotropy $g$ which yields values close to unity for small scattering angles). The physical interpretation is that for highly forward directed scattering (small $\theta_{\mathrm{rms}}$, $g$ close to unity), the shape of the forwarded scattered beam is only marginally altered on subsequent scattering events. Thus, it remains possible for this beam to be coupled back in to the OCT system, leading a large contribution of multiple forward scattered light. The contribution of multiple scattered light will show as an overall signal decay that is slower than the single backscattered light, e.g., $\mu_{\mathrm{OCT}} < \mu_S$. If the scattering is more isotropic (larger $\theta_{\mathrm{rms}}$, $g \ll 1$), each subsequent scattering event considerably broadens the forward scattered beam. This reduces the coupling efficiency of that beam and subsequently the contribution of multiple scattered light will be less; leading to a measured $\mu_{\mathrm{OCT}}$ much closer to $\mu_S$.

## 3 Methods

The OCT data were recorded with the Santec IVS 2000 swept-source OCT system, at a center wavelength of $\lambda_0 = 1309$ nm, ~140-nm sweep range, with a sweep rate of 50 kHz. Optical and sampling resolutions were approximately equal at $\Delta k_{\mathrm{OPTICAL}} \approx \Delta k_{\mathrm{SAMPLING}} \approx 0.0003\ \mu\mathrm{m}^{-1}$. From a knife-edge measurement, the diameter of the collimated beam was measured at $2.54 \pm 0.01$ mm. The NA of the system was 0.02 with a focal length of 65 mm, and the Rayleigh length measured in air was 960 $\mu$m. The mode field diameter of the fiber was 2.9 $\mu$m. The position of the focus was coaligned with the position of the reference mirror (zero-delay). The combined sensitivity roll-off, expressed as the depth where the signal drops to −3 dB of its initial value, was ≈3.8 mm. The measured axial and lateral resolutions were 12 and 25.5 $\mu$m in air, respectively. A cross-section image (B-scan) was built from 1000 adjacent A-lines. The samples were measured in a 1-mm quartz cuvette. The inner boundary of the cuvette was placed at $z_0 = 650\ \mu$m $\pm 34\ \mu$m from zero delay. The cuvette was placed under an angle of ~10 deg to avoid specular reflection from the boundary.

### 3.1 *System Parameter Calibration*

All recorded data were corrected for system-induced attenuation, i.e., caused by the confocal PSF and sensitivity roll-off as described in Sec. 2. Due to the low NA and high spectral resolution of our system, both are slowly decaying functions of depth and can in practice be approximated by a single exponential decay with attenuation constant $\mu_{\mathrm{CAL}}$. Thus, Eq. (1) can be modified to

$$\langle A^2(z)\rangle \approx \alpha \cdot \exp(-2\mu_{\mathrm{CAL}} z) \cdot \mu_{B,\mathrm{NA}} \exp[-2\mu_{\mathrm{OCT}}(z - z_0)]. \tag{11}$$

The $\mu_{\mathrm{CAL}}$ can straightforwardly be obtained from an OCT measurement of a very weakly scattering sample. We used a 1000-fold dilution of Intralipid 20% in water, for which the scattering coefficient at our center wavelength is estimated to be $\mu_{S,IL} \approx 0.01\ \mathrm{mm}^{-1}$. The fitted signal attenuation corresponding to $\mu_{\mathrm{CAL}}$ was found to be 1.1 $\mathrm{mm}^{-1}$ for this system. Note that the absorption of water (from literature: 0.135 $\mathrm{mm}^{-1}$)[25] is also accounted for in this manner.

### 3.2 *Sample Preparation*

Monodisperse silica beads (Kisker Biotech, Steinfurt, Germany) with measured mean diameters of 0.47, 0.70, 0.91, and 1.60 $\mu$m were suspended in distilled water for a monodisperse concentration series. For an accurate measurement of the size distribution, the silica beads were imaged using transmission electron microscopy (TEM) (Philips CM-10) (Fig. 2). The TEM images were acquired and analyzed following the protocol described in previous work.[10] The obtained values of the mean diameter and standard deviation of the bead sizes are shown in Table 1. To prevent aggregation of the beads in suspension, 0.03 mM of sodium dodecyl sulfate was added to all samples.[26] The 0.47- and 0.70-$\mu$m sized beads were diluted to 10 samples with volume fractions ranging from 0.02 to 0.2. The 0.91- and 1.60-$\mu$m sized beads were diluted to 5 samples with volume fractions from 0.02 to 0.1. Suspensions with a higher volume fraction of silica were not studied due to aggregation of the beads. All samples were 4 to 6 times alternatingly vortexed and sonicated for 15 min.

### 3.3 *Optical Coherence Tomography Data Analysis*

We used a custom-written code (LABVIEW 2013, National Instruments) for the analysis of the acquired OCT data. The attenuation ($\mu_{\mathrm{OCT}}$) was obtained from the data by NLLS fit of a single exponential decay model $y = \mathrm{AMP} * \exp(-\mu z) + y_0$ to the OCT signal in depth. The data were first averaged over at least 1000 A-lines. The selection of the fit was done manually where the start region was chosen to approximately be 50 $\mu$m behind the cuvette boundary. The end point of the fit was chosen such that within the ROI, upon visual inspection, the signal appeared to follow a single exponential decay curve. An offset added to the fit model was fixed at the average noise level directly at the backside of the cuvette. The amplitude and decay constant $\mu$ were independently varied parameters. The fit was repeated 100 times, during which the boundaries of the ROI were varied within 10% of their operator-selected

**Table 1** Mean and standard deviation of the size distribution of monodisperse silica beads measured with transmission electron microscopy.

| Monodisperse silica beads (Kisker Biotech) | Mean diameter ($\mu$m) | Standard deviation ($\mu$m) |
|---|---|---|
| PSI 0.5 | 0.47 | 0.03 |
| PSI 0.8 | 0.70 | 0.03 |
| PSI 1.0 | 0.91 | 0.02 |
| PSI 1.5 | 1.60 | 0.03 |

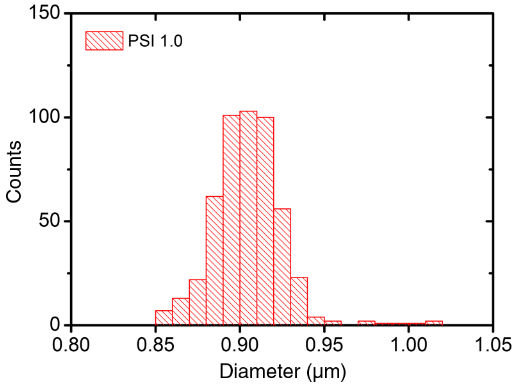

**Fig. 2** Histogram of the size distribution of monodisperse silica beads (PSI 1.0) measured with transmission electron microscopy.

values. The mean value of the 100 measurements was taken as the final $\mu$ value, with uncertainty estimated as the standard deviation of the fits. The obtained attenuation $\mu$ was corrected for system parameters, as described in Sec. 3.1, yielding $\mu_{\mathrm{OCT}} = \mu - \mu_{\mathrm{CAL}}$.

The backscattering coefficient, $\mu_{B,\mathrm{NA}}$, was determined from the amplitude of the backscattered OCT signal[18,19] in a superficial ROI starting at $z_{\mathrm{ROI}} = 0.03$ mm below the glass–sample interface. The ROI is chosen as such to exclude contribution of multiple scattered light. The region extends only 0.026 mm (4 pixels) in depth to minimize the effects of attenuation, which was verified by ensuring that the OCT amplitude speckle contrast in the ROI was 0.52,[27] corresponding to fully developed speckle, which can only be achieved if no appreciable attenuation in depth takes place in the ROI.[28] By Eq. (11), in this ROI, we have $\langle A^2(z_{\mathrm{ROI}})\rangle = \alpha \exp(-\mu_{\mathrm{CAL}} z_{\mathrm{ROI}})\mu_{B,\mathrm{NA}}$ which features only system-dependent parameters. This allows us to define a scaling factor between measured amplitude and backscatter coefficient $\mu_{B,\mathrm{NA}} = sf_{\varnothing}\langle A^2(z_0)\rangle$, where the scaling factor is determined separately for each particle diameter using the highest volume fraction $f_{v\mathrm{MAX}}$: $sf_{\varnothing} = [\mu_{B,\mathrm{NA(MIE-PY)}}/\langle A^2(z_0)\rangle]_{\varnothing, f_{v\mathrm{MAX}}}$.

## 3.4 *Multiple Scattering*

A practical approach for assessing the influence of multiple scattering for confocal reflectance microscopy and OCT was proposed by Jacques et al.[22] Based on Monte Carlo simulation, a reference grid is constructed, allowing for the mapping of scattering the coefficient and scattering anisotropy to the amplitude and decay rate and *vice versa*.[22,29] We adopt this approach, but rather than relying on Monte Carlo simulations, we use the analytical EHF model proposed in Sec. 2.3 to simulate the OCT signal at a range of values of the scattering coefficient and anisotropy and, subsequently, fit the single exponential decay to the simulated signal to retrieve the corresponding predicted value of $\mu_{\mathrm{OCT}}$. This procedure is illustrated in Fig. 3.

## 3.5 *Calculations*

To calculate predictions for $\mu_{\mathrm{OCT}}$ and $\mu_{B,\mathrm{NA}}$, we have written a Labview code (Labview 2013, National Instruments). We implemented Mie calculations from Ref. 30 and calculated the differential scattering cross section for each particle by integrating over the size distribution measured with TEM (Table 1 and Fig. 2). The refractive index of the silica beads was fixed at 1.425 (within the range provided by the manufacturer) and converted to 1309 nm using the dispersion curve from Malitson[31] ($n = 1.419$ to 1.449). The refractive index of the medium was assumed to be equal to that of water (1.324).[32] The Percus–Yevick structure factor $S(\theta)$ was calculated in Ref. 24, using volume fraction and mean particle diameter (Table 1) as input parameters. By combining the Mie-calculated $\sigma_S(\theta)$ with this structure factor, we calculate $\mu_S$ [Eq. (6)], $\mu_{B,\mathrm{NA}}$ [Eq. (7)], and rms scattering angle $\theta_{\mathrm{rms}}$ for each sample

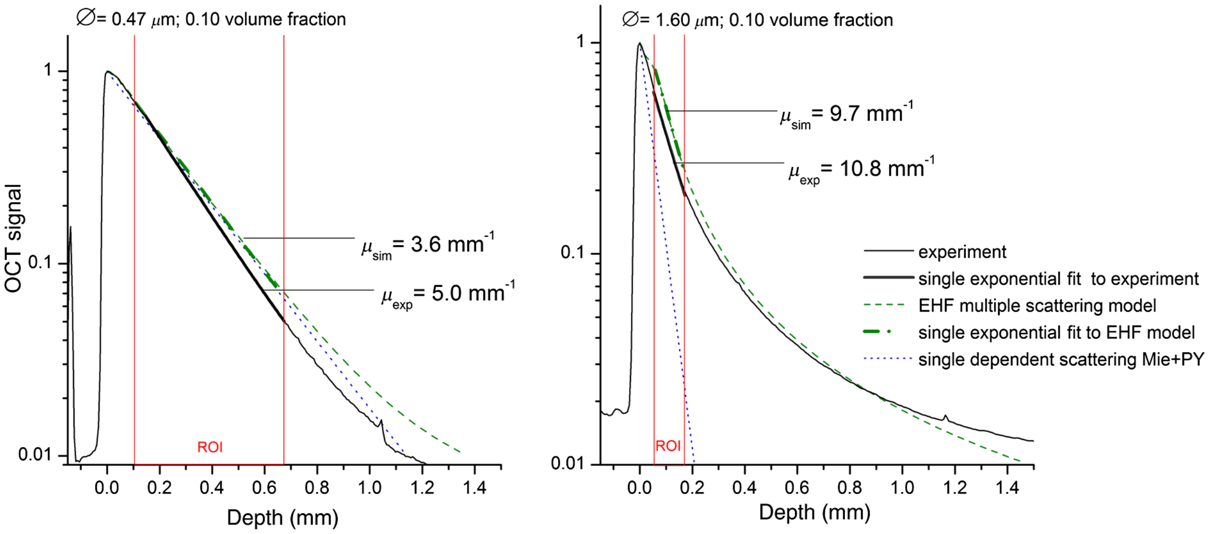

(a) (b)

**Fig. 3** Simulated extended Huygens–Fresnel (EHF) model for optical coherence tomography (OCT) (green dashed line), experimental OCT curve (black solid line) fitted with a single exponential decay within the ROI for samples of 0.1 volume fraction: (a) 0.47-$\mu$m beads and (b) 1.60-$\mu$m beads. The simulated single scattering (Mie + PY) curve (blue dotted line) is plotted for reference. The exponential decay of the fits on the experimental curves is (a) $\mu_{\mathrm{exp}} = 5.0$ mm$^{-1}$ and (b) $\mu_{\mathrm{exp}} = 10.8$ mm$^{-1}$. After correction of system-induced attenuation ($\mu_{\mathrm{CAL}} = 1.1$ mm$^{-1}$), the decay rates match closely with the decay of the simulated curves: (a) $\mu_{\mathrm{sim}} = 3.6$ mm$^{-1}$ and (b) $\mu_{\mathrm{sim}} = 9.7$ mm$^{-1}$.

(Mie + PY). The EHF calculations were based from Ref. 12 and took the system properties center wavelength, focal length, and Rayleigh length as input parameters, as well as the medium refractive index and the $\mu_S$ and $\theta_{\mathrm{rms}}$ (MIE + PY) for each sample. To quantify the accuracy of the prediction, for each model, the standard error of the estimate ($s$) was calculated as $\sqrt{\sum(\mu_{\mathrm{OCT,EXPERIMENTAL}} - \mu_{\mathrm{OCT,PREDICTION}})^2/N}$, where $N$ is the number of data points (volume fractions). The lower $s$ corresponds to a better predictive value. An uncertainty estimate on $s$ was calculated using a bootstrapping method,[33] we calculate $N$ values of $s$ from an $(N-1)$ sized dataset by leaving out each value of the original dataset once. The standard deviation of the resulting sequence of $s$-values is taken as an uncertainty estimate (Table 2). A similar analysis was performed for the backscattering coefficient (Table 3).

## 4 Results

The experimental data points and predicted calculated curves of $\mu_{\mathrm{OCT}}$ as a function of volume fraction of silica beads are plotted in Fig. 4 (ranging from 1 to 10 $\mathrm{mm}^{-1}$). In every graph, the calculated curves of $\mu_{\mathrm{OCT}}$ using Mie theory (single, concentration-independent scattering), Mie + PY (single, concentration-dependent scattering), and Mie + PY + EHF (concentration dependent and multiple scattering) models are plotted for reference. To quantitatively evaluate the match between experimental data and the theoretical predictions for $\mu_{\mathrm{OCT}}$, the standard error of the estimate is calculated (Table 2). For the beads with a mean diameter of 0.47 and 0.70 $\mu$m, the experimental values of $\mu_{\mathrm{OCT}}$ are well described by the calculated single scattering curve, in which concentration-dependent scattering properties of the phantoms are accounted for by combining Mie theory with the Percus–Yevick radial distribution (Mie + PY). No contribution of multiple scattered light is observed for the smallest beads (0.47 $\mu$m). For the 0.70-$\mu$m beads, multiple scattering contributes only at high volume fractions for which $\mu_S$ is high. For the beads with a diameter of 0.91 $\mu$m and corresponding intermediate forward scatter (scattering anisotropy $g \approx 0.8$), we see a significant contribution of multiple scattering for the higher volume fractions of scatterers. For the beads with a mean diameter of 1.60 $\mu$m and corresponding larger forward scatter (high scattering anisotropy $g \approx 0.9$), we see a significant contribution of multiple scattered light. By combining Mie+PY with the EHF model, we are able to accurately describe the contribution of multiple scattering as the experimental data points and calculated curves (Mie + PY + EHF) are in good agreement. To illustrate the influence of concentration-dependent scattering on the scattering anisotropy, we plotted the scattering anisotropy ($g$) of the samples, as calculated with Mie theory and Mie + PY as a function of volume fraction in Fig. 5. This figure shows the influence of the concentration of scatters on the average cosine of the scattering angle. The weighting by the concentration-dependent structure factor leads to relatively more backscatter and thus a decrease in scattering anisotropy with increasing volume fraction. This effect is more pronounced for smaller sized beads. Figure 6 shows the experimental data points and calculated curves of the backscattering coefficient, $\mu_{B,\mathrm{NA}}$, as a function of volume fraction calculated with Mie + PY. Per bead size, a scaling factor is used to scale experimental amplitudes to $\mu_{B,\mathrm{NA}}$ (Sec. 3.3), which takes into account the system-dependent parameters. The curves calculated with only Mie scattering (no concentration-dependent scattering) are plotted as a reference. The values of the standard error of the estimate are shown in Table 3. The experimental data points and calculated Mie + PY curves are in good agreement.

**Table 2** The standard error of estimates is calculated to evaluate the match between the experimental data and the theoretical predictions for $\mu_{\mathrm{OCT}}$ by the three models (Mie, Mie–PY, and Mie–PY–EHF). Uncertainties are estimated using a bootstrapping method.

| ∅ | MIE | MIE–PY | MIE–PY–EHF |
|---|---|---|---|
| 0.47 | 2.7 (±0.2) | 0.29 (±0.02) | 0.24 (±0.02) |
| 0.70 | 4.7 (±042) | 0.41 (±0.02) | 0.51 (±0.02) |
| 0.91 | 2.7 (±0.5) | 0.7 (±0.1) | 0.35 (±0.06) |
| 1.60 | 11 (±2) | 7 (±1) | 0.36 (±0.06) |

**Table 3** The standard error of estimates is calculated to evaluate the match between the experimental data and the theoretical predictions for $\mu_{B,\mathrm{NA}}$ by the two models (Mie and Mie–PY). Uncertainties are estimated using a bootstrapping method.

| ∅ | MIE | MIE–PY |
|---|---|---|
| 0.47 | $2.1(\pm 0.2) \times 10^{-5}$ | $5.9(\pm 0.6) \times 10^{-6}$ |
| 0.70 | $6.3(\pm 0.3) \times 10^{-7}$ | $2.7(\pm 0.1) \times 10^{-7}$ |
| 0.91 | $3.2(\pm 0.1) \times 10^{-6}$ | $3.1(\pm 0.1) \times 10^{-6}$ |
| 1.60 | $4.4(\pm 0.3) \times 10^{-7}$ | $4.4(\pm 0.3) \times 10^{-7}$ |

## 5 Discussion

We describe a method that validates measurement of OCT-derived attenuation coefficient $\mu_{\mathrm{OCT}}$ which is correlated to tissue disease state in various clinical studies, ranging from ophthalmology,[34] cardiology,[2] dermatology,[6] to urology.[35,36] Paramount to clinical relevance is understanding how $\mu_{\mathrm{OCT}}$ depends on properties of the OCT system itself, as well as the influence of multiple scattering by tissue properties: only then can reproducible results be obtained either with the same OCT system or by different systems. Therefore, we described the influence of the confocal PSF and sensitivity roll-off in depth [Eq. (1)] and introduced a practical method to calibrate their influence (Sec. 3.1) for commonly applied, low-NA clinical systems. Furthermore, we describe DRM for calibration of $\mu_{\mathrm{OCT}}$ with tissue-mimicking scattering properties ($\mu_{\mathrm{OCT}}$ between 1 to 10 $\mathrm{mm}^{-1}$ and $g$ between 0.4 and 0.9).

### 5.1 *Concentration-Dependent Scattering Versus Multiple Scattering*

For higher scattering coefficients and low values of $\theta_{\mathrm{rms}}$ ($\sim g$ close to 1), multiple forward scattered light has a large contribution to the OCT signal. Corresponding DRM for calibration purposes requires high volume fraction of the scatterers. However, for high volume fractions, the bulk optical properties of the DRM cannot be extrapolated from the optical properties of a single scatterer simply through scaling by volume fraction. Rather than adding scattered intensities, scattered fields (amplitude and phase) from the individual particles in the DRM should be added (taking into account their interference) to calculate the optical properties. This situation is commonly referred to as

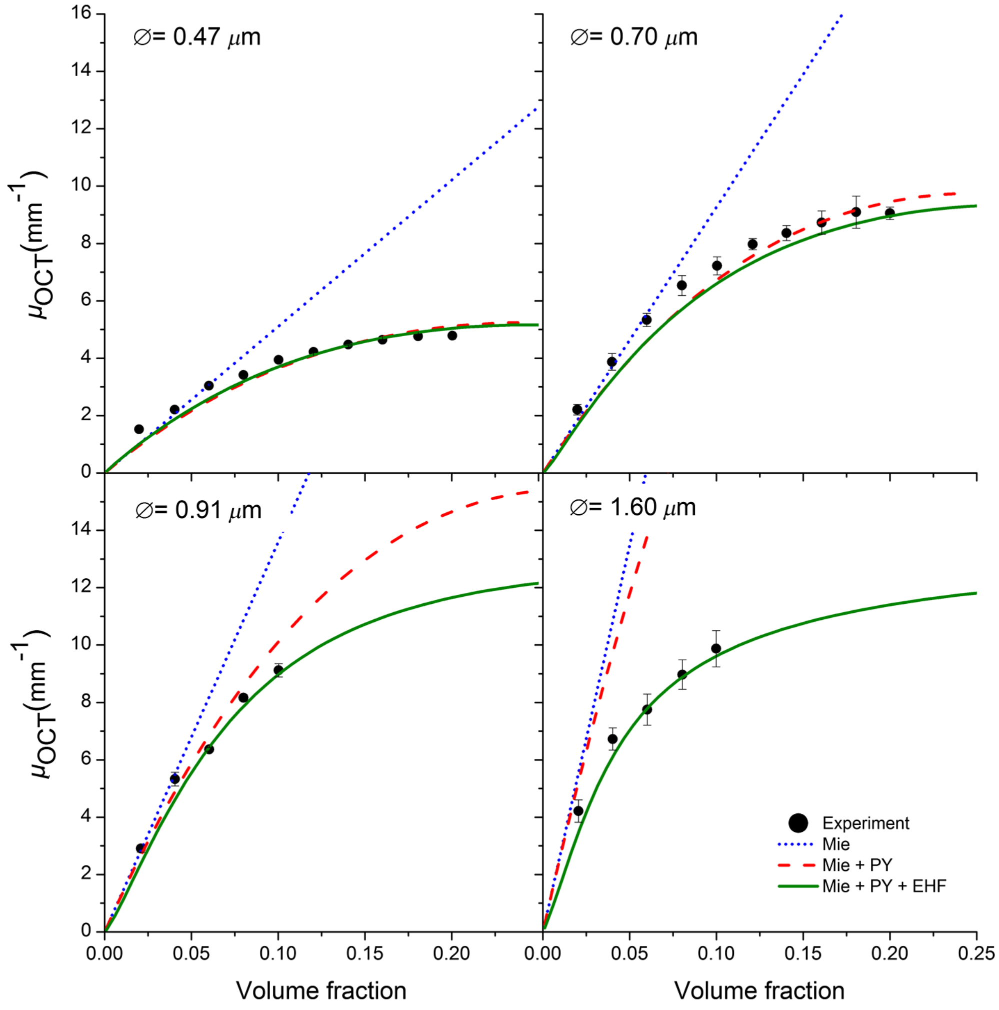

**Fig. 4** The volume-fraction dependence of the OCT attenuation coefficient, $\mu_{\mathrm{OCT}}$, of four different sized silica beads (mean diameter: 0.47, 0.70, 0.91, and 1.60 $\mu$m). The black dots depict the experimental data point and the error bars depict the uncertainty estimated as the standard deviation of 100 fits. The plotted curves show the calculated data. The blue dotted lines are the Mie calculations, the red dashed lines are the Mie calculations combined with Percus–Yevick formalism (Mie + PY) to include concentration-dependent scattering, and the green lines are the calculations combining Mie + PY with the EHF model to account for multiple scattering.

"concentration-dependent scattering" as the bulk optical properties now depend nonlinearly on volume fraction. The effect of concentration-dependent scattering is that the scattering coefficient $\mu_S$ scales as a lower-than-linear rate with volume fraction [$\mu_S < (f_V/V_P)\sigma_{\mathrm{SCAT}}$]; Sec. 2.2), leading to a lower $\mu_{\mathrm{OCT}}$ compared with the "concentration-independent scattering" case. Increased detection of multiple-forward scattering leads to further reduction of $\mu_{\mathrm{OCT}}$. Therefore, care must be taken to separate both effects in data analysis. Here, we predict $\mu_{\mathrm{OCT}}$ by first calculating $\mu_S$ and $\theta_{\mathrm{rms}}$ for our DRM samples by using Mie theory (scattering properties of individual spheres) and the Percus–Yevick structure factor (concentration-dependent scattering). These values are then input to the EHF equation that describes the OCT signal in the multiple scattering regime. $\mu_{\mathrm{OCT}}$ is derived by fitting a single exponent to the simulated data. The measured values for $\mu_{\mathrm{OCT}}$ correspond closely to these predictions (Fig. 4). For samples with a low amount of forward scattering (low $g$-value, Fig. 5), no contribution of multiple scattered light is observed. Although the EHF model is limited by the paraxial approximation, its prediction does not deviate from the concentration-dependent scattering curve and is in good agreement with the experimental data, which suggests a broad applicability of the EHF model. For the case of weakly scattering media with moderate scattering anisotropies, the simpler Mie–Percus–Yevick model may be used for accurate prediction of $\mu_{\mathrm{OCT}}$. The backscattering coefficient, $\mu_{B,\mathrm{NA}}$, is best predicted by Mie–Percus–Yevick theory for all particle sizes. Even though no statistical difference is found between the prediction based on Mie theory or Mie–Percus–Yevick theory, only the latter model yields accurate predictions for both parameters. The physical explanation is that, as the volume fraction increases, the increment in scattering coefficient decreases [e.g., the integral part of Eq. (6) is a decreasing function of volume fraction] while at the same time increasingly more light is scattered to the backward direction [e.g., the integral part of Eq. (7) remains almost constant]. Effectively, the backscattering coefficient scales linearly with volume fraction in both models.

We conclude that our approach correctly separates the contributions of concentration dependent and multiple scattering, substantiated by the correct prediction of the backscattering coefficient $\mu_{B,\mathrm{NA}}$ from the same calculations (Fig. 6). We measure $\mu_{B,\mathrm{NA}}$ at depths in the order of 1 mean free path to

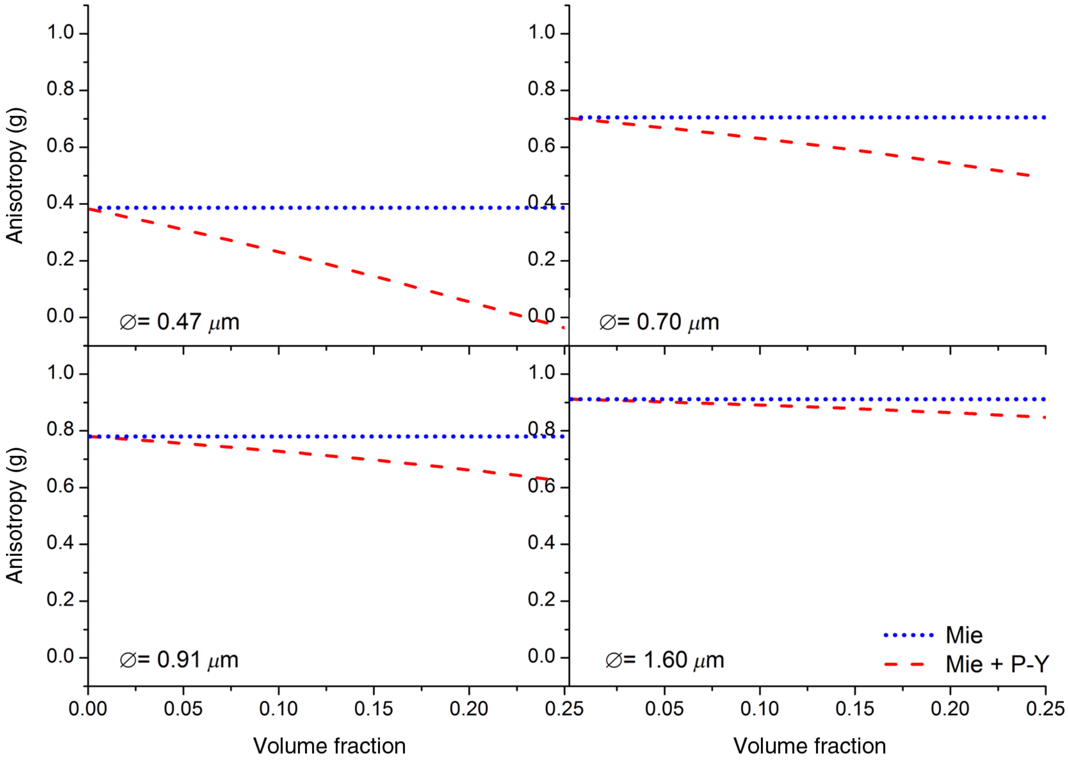

**Fig. 5** The calculated scattering anisotropy (*g*) of the silica beads as a function of their volume fractions. The blue dotted lines are the single, concentration-independent scattering, Mie, calculations. The red dashed lines are the single, concentration-dependent scattering calculation, where Mie theory is combined with the Percus–Yevick PCF (Mie + PY). A change in scattering anisotropy as a function of volume fraction is predicted when comparing Mie + PY (single, concentration-dependent scattering) to Mie (single, concentration-independent scattering) calculations.

minimize attenuation of the signal within the ROI (minimum mean free path is $\mu_S^{-1} = 30\ \mu\text{m}$ for $\varnothing = 1.60$-$\mu$m particles, volume fraction = 0.1). Moreover, we have recently demonstrated correct prediction of scattering coefficients $\mu_S$ by Mie–Percus–Yevick theory, using transmission-based low-coherence interferometry.[10] In that experiment, the contribution of small-angle multiple forward scattering is greatly reduced by probing only the ballistic light transmitted through the sample.

The weighting of the differential scattering cross section with the structure factor (concentration-dependent scattering) also leads to more light being scattered into the backward direction. Ultimately, these two contrary effects result in an almost linear increase of the backscattering coefficient $\mu_{B,\text{NA}}$ with volume fraction. Clearly, this result is not general but depends on the exact scattering phase function of the used sample/tissue and the confocal configuration of the OCT system as predicted by the presented theory.

To eliminate contributions of multiple scattering, Xu et al.[13] propose to confine the ROI of the fit between $I_{\max}$ and $I_{\max}/\text{e}$. As can be seen from the EHF equations [Eqs. (8)–(10)], the multiple scattering starts to contribute directly from $z = z_0$, or $\Delta z = (z - z_0) = 0$. The nonscattered beam attenuates with $\exp(-\mu_s \Delta z)$ and the (small angle, forward) scattered beam grows in intensity with $[1 - \exp(-\mu_s \Delta z)]$. This latter beam, however, broadens upon propagation [Eq. (10)], so that coupling back into the single-mode fiber of the OCT system will become more difficult with increasing $\Delta z$. The contribution of multiple scattering, therefore, is a balance between these two factors. At small values of $\Delta z$, the power in the scattered beam is small but, since the spread (increased divergence of the scattered beam) is small, it is more effectively coupled back. In contrast, for larger values of $\Delta z$, the power in the scattered beam is increased, but due to the increased spread, the coupling efficiency is worse. At very large depths, the highly increased magnitude of the scattered beam starts to dominate the single-backscattered contribution.

Two solutions proposed in literature are commonly adopted to take into account the multiple scattered light contribution to the OCT signal: the EHF model described here and a Monte Carlo derived model introduced by Jacques et al.[22] We have adopted the EHF model in this work, but adjusted for the confocal PSF for a diffuse reflection, where we assume that the lateral phase of the probing beam is lost upon reflection. In practice, this is accounted for by setting the Rayleigh length in the medium to 2 times the value measured for specular reflection (Sec. 2.3).[15,20] In the other approach, an empirical equation is derived by Monte Carlo simulations to approximate the contribution of multiple scattering.[22,29] Levitz et al.[29] use this approach and translate $\mu_{\text{OCT}}$ and amplitude to $\mu_S$ and $g$ based on calibration of the peak signal of a known interface (scattering phantom with known optical properties). The strength of our approach is that the variation of any parameter in the model may be changed easily to study its influence on the retrieved optical properties (of course, within the range of validity of the model itself, e.g., dominant forward scattering). The empirical model by Jacques et al.[22] would require a new set of simulations if, for example, the detection NA changes. In concept, however, both methods are equivalent in that the mapping function $f(\mu_S)$ in Eq. (1) is studied either using an analytical model or Monte Carlo simulations.

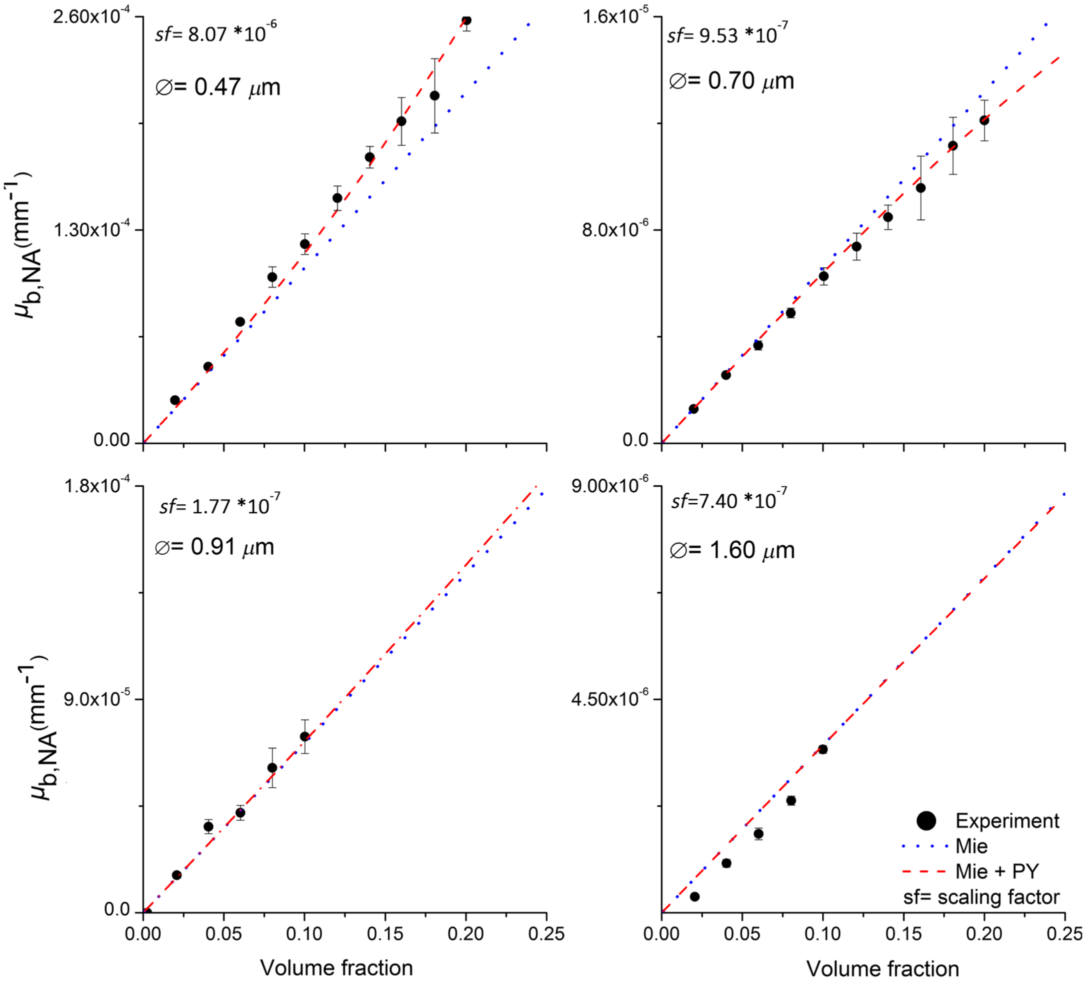

**Fig. 6** The volume-fraction dependence of the backscattering coefficient ($\mu_{B,\mathrm{NA}}$). The black dots show the experimental data points and the error bars depict the standard deviation from five independent measurements. The blue dotted lines are the single, independent scattering, Mie calculations. The red dashed lines are the single, concentration-dependent scattering, Mie + PY calculations. Here, we do not include any multiple scattering, as the experimental data are taken in a thin superficial layer to minimize the contribution of multiple scattered light. A scaling factor ($sf$) [$sf_{\varnothing} = [\mu_{B,\mathrm{NA}\,(\mathrm{MIE-PY})}/\langle A^2(z_0)\rangle]_{\varnothing,f_{v\mathrm{MAX}}}$] is used to obtain $\mu_{B,\mathrm{NA}}$ from $A$. Per particle size, we used the measurement at highest volume fraction to calculate the scaling factor.

### 5.2 *Limitations and Clinical Implications*

Our model calculations assume applicability of Mie–Percus–Yevick calculations to account for concentration-dependent scattering and the EHF model to account for multiple small-angle forward scattering. Input for the Mie–Percus–Yevick calculations is size and refractive index of the silica spheres making up the DRM. In our present calculations, we use the mean diameter of the size distribution as measured by TEM. Alternatively, an effective "scattering diameter" can be computed by weighting the size distribution with the corresponding scattering cross sections which yield only small deviations from our present calculations (<1% in $\mu_{\mathrm{OCT}}$). By averaging over all particle sizes, we can draft a rule of thumb expression for the concentration-dependent scattering coefficient $\mu_S$ as a function of volume fraction $f_V$ and the concentration-independent scattering cross section $\sigma_{S,\mathrm{MIE}}$ of particles with volume $V_P$:

$$\mu_S \approx (1 - 2.4\{\pm 0.2\} f_v)\frac{f_v}{V_P}\sigma_{S,\mathrm{MIE}},$$

which is intriguingly similar to the result obtained for blood[37] (see below).

Since the specified uncertainty of the refractive index of silica beads is 2%, we have selected the refractive index ($n = 1.425$) that describes all measured data most accurately. To study how the refractive index affects the calculations, we have varied the optimal refractive index with 1% (not shown here). This resulted in a maximum uncertainty in $\mu_{\mathrm{OCT}}$ of 20% for 0.70 $\mu$m spheres at 0.2 volume fraction ($\mu_{\mathrm{OCT}}$ $8.9 \pm 1.8\ \mathrm{mm}^{-1}$).

An alternative approach to determining $\mu_{\mathrm{OCT}}$ would be direct fitting of the EHF model [Eq. (8)] to the OCT signal in depth to obtain $\mu_S$ and $\theta_{\mathrm{rms}}$. However, this is not always possible because $\mu_S$ and $\theta_{\mathrm{rms}}$ (via $w_S$) are competing parameters: change in one of the parameters can often be compensated by a change in the other leading to different sets of ($\mu_S$, $\theta_{\mathrm{rms}}$) with equivalent statistical goodness of fit. The resulting curve fit may, therefore, not always converge to realistic values.[15] A promising venue to be explored in future studies is the combination of OCT with other (fiber-based) technologies such as single-fiber reflectance spectroscopy[38] that can provide independent parameterization of the scattering phase function—and thus in principle of $\theta_{\mathrm{rms}}$.

We calculate the amplitude directly from the OCT data and do not use the amplitude from the fitted A-scans. A practical concern is that in many cases of interest, such as epithelial tissues, the number of data points is limited for an NLLS curve fit. With a common OCT resolution of 10 $\mu$m, and for example a layer thickness of 50 $\mu$m, only five unique data points are available, which may lead to inconclusive fitting results on $\mu_{\mathrm{OCT}}$ and $\mu_{B,\mathrm{NA}}$. We scaled the measured OCT signal amplitude to the backscattering coefficient, $\mu_{B,\mathrm{NA}}$, within the system's NA using a scaling factor that was calculated at the highest volume fraction. Ideally, a single calibration factor could be used for scaling.[10] In (clinical) practice, however, the scaling is influenced by parameters that may change between measurements, for example, when switching disposable probes with slightly different coupling efficiencies. In practice, it is, therefore, desirable to calibrate each probe/measurement individually using phantoms with known scattering properties. In this work, it required calibration for each volume-fraction series, per particle diameter.

To obtain quantitative measurement of OCT-derived parameters $\mu_{\mathrm{OCT}}$ and $\mu_{B,\mathrm{NA}}$, it is crucial to calibrate for system parameters (confocal PSF and sensitivity roll-off). However, the contribution of multiple scattering is challenging to quantify. From Fig. 4, we conclude that multiple scattering starts to have a large (>10%) effect on the measured $\mu_{\mathrm{OCT}}$ for samples with a high anisotropy, $g > 0.8$, and high scattering coefficient, $\mu_S > 10\ \mathrm{mm}^{-1}$. In this case, it is advisable to consider multiple scattering to map $\mu_{\mathrm{OCT}}$ to $\mu_S$. For samples with lower anisotropy factor and scattering cross-section, values of $\mu_S$ are within 10% variation of $\mu_{\mathrm{OCT}}$.

The role of concentration-dependent scattering is absent for tissue, since this only relates to upscaling optical properties of individual scatterers to those of a solution of scatterers at a given volume fraction. In general, both "an individual scatterer" and "volume fraction" cannot be defined for biological tissue. Instead of a DRM, tissue is arguably better described as a continuous random medium,[39] where statistical properties, such as variance, correlation length, and fractal dimension of the spatial refractive index fluctuation, take the role of refractive index contrast, correlation length of Percus–Yevick PCF, and particle size that describes the DRM. Linking these different sets of parameters to OCT measured optical properties will be subject of further research, deploying increasingly hybrid samples (duo and polydisperse bead mixtures of known size distribution).[40]

The exceptional biological specimen for which scattering properties may indeed be described by the Mie–Percus–Yevick formalism, is whole blood. The main scatterers (red blood cells) can be regarded as spherical when sufficient averaging over orientation is possible (validating the use of Mie theory).[41] The physiological volume fraction ($f_V \sim 0.45$) is sufficiently high to warrant the use of the Percus–Yevick structure factor. In a recent theoretical study annex literature review, we found that $\mu_s \sim (1 - f_V)^2 (f_V / V_{\mathrm{RBC}}) \sigma_{\mathrm{SCAT}}$ as opposed to $\mu_s = (f_V / V_{\mathrm{RBC}}) \sigma_{\mathrm{SCAT}}$ for concentration-independent scattering.[37] Specifically, the predicted scattering coefficient and scattering anisotropy $g$ at 800 nm are $\mu_s = 71\ \mathrm{mm}^{-1}$, $g = 0.9812$; $\mu_A = 0.38\ \mathrm{mm}^{-1}$ and $\mu_s = 63\ \mathrm{mm}^{-1}$, $g = 0.9820$; $\mu_A = 0.47\ \mathrm{mm}^{-1}$ for oxygenated and deoxygenated blood, respectively. The major contribution of multiple forward scattered light in this case resulted in the highly decreased contribution of scattering properties to the total OCT attenuation coefficient, e.g., measured $\mu_{\mathrm{OCT}}$ of 5.5 and 5.8 $\mathrm{mm}^{-1}$ for oxygenated and deoxygenated blood, respectively.[42] Accurate separation of scattering and absorption contributions to $\mu_{\mathrm{OCT}}$ may enable quantitative OCT-based measurement of $\mu_A$ (spectra) leading to quantification of localized oxygen saturation. Previously, we raised the question of whether quantitative measurements of attenuation by blood coefficients by OCT are feasible[43] and concluded that better modeling of the concentration-dependent OCT signal was needed. With the theoretical results presented in Ref. 37 and the experimental validation of the influence of light scattering described in this contribution, accurate determination of attenuation by blood, and subsequent extraction of oxygen saturation, seems feasible and warrants further experimental validation studies.

## 6 Conclusions

We propose a comprehensive model of the OCT signal accounting for the influence of the confocal PSF and sensitivity roll-off together with an experimental procedure from which the amplitude $\mu_{B,\mathrm{NA}}$ and decay constant $\mu_{\mathrm{OCT}}$ can be quantified. Both experimental quantities have been investigated as markers of disease (progression) in various medical fields. We validate their quantification using OCT measurements of DRM consisting of silica spheres within a wide range of scattering properties. We show that such validation measurements over the range of scattering properties found in tissue require DRM of high volume fractions, for which concentration-dependent scattering and multiple scattering effects cannot be neglected. We, therefore, include the Percus–Yevick structure factor and the EHF formalism in our model and demonstrate excellent agreement between predicted and measured values of $\mu_{\mathrm{OCT}}$ and $\mu_{B,\mathrm{NA}}$ versus volume fraction.

## *Acknowledgments*

This research was funded as part of the IOP Photonic Devices, Project number IPD 12020, managed by the Netherlands Enterprise Agency, and was performed within the framework of Institute Quantivision, a collaboration initiative of AMC, NKI, UvA, VU, and VUmc. We thank E. van de Pol, PhD, for the size determination of the silica beads.

## *References*

1. R. A. McLaughlin et al., "Parametric imaging of cancer with optical coherence tomography," *J. Biomed. Opt.* **15**(4), 046029 (2010).
2. G. van Soest et al., "Atherosclerotic tissue characterization in vivo by optical coherence tomography attenuation imaging," *J. Biomed. Opt.* **15**(1), 011105 (2010).
3. R. Wessels et al., "Optical coherence tomography in vulvar intraepithelial neoplasia," *J. Biomed. Opt.* **17**, 116022 (2012).
4. L. Scolaro et al., "Parametric imaging of the local attenuation coefficient in human axillary lymph nodes assessed using optical coherence tomography," *Biomed. Opt. Express* **3**(2), 366 (2012).
5. T. Xie, M. Zeidel, and Y. Pan, "Detection of tumorigenesis in urinary bladder with optical coherence tomography: optical characterization of morphological changes," *Opt. Express* **10**(24), 1431–1443 (2002).
6. R. Wessels et al., "Functional optical coherence tomography of pigmented lesions," *J. Eur. Acad. Dermatol. Venereol.* **29**(4), 738–744 (2015).
7. Y. Yang et al., "Optical scattering coefficient estimated by optical coherence tomography correlates with collagen content in ovarian tissue," *J. Biomed. Opt.* **16**(9), 090504 (2011).
8. E. C. C. Cauberg et al., "Quantitative measurement of attenuation coefficients of bladder biopsies using optical coherence tomography for

grading urothelial carcinoma of the bladder," *J. Biomed. Opt.* **15**(6), 066013 (2010).
9. J. K. Percus and G. J. Yevick, "Analysis of classical statistical mechanics by means of collective coordinates," *Phys. Rev.* **110**(1), 1–13 (1958).
10. V. D. Nguyen et al., "Dependent and multiple scattering in transmission and backscattering optical coherence tomography," *Opt. Express* **21**(24), 29145–29156 (2013).
11. J. M. Schmitt and A. Knüttel, "Model of optical coherence tomography of heterogeneous tissue," *J. Opt. Soc. Am. A* **14**(6), 1231 (1997).
12. L. Thrane, H. T. Yura, and P. E. Andersen, "Analysis of optical coherence tomography systems based on the extended Huygens-Fresnel principle," *J. Opt. Soc. Am. A* **17**(3), 484 (2000).
13. C. Xu et al., "Characterization of atherosclerosis plaques by measuring both backscattering and attenuation coefficients in optical coherence tomography," *J. Biomed. Opt.* **13**(3), 034003 (2008).
14. T. G. Van Leeuwen, D. J. Faber, and M. C. Aalders, "Measurement of the axial point spread function in scattering media using single-mode fiber-based optical coherence tomography," *IEEE J. Sel. Top. Quantum Electron.* **9**(2), 227–233 (2003).
15. D. J. Faber et al., "Quantitative measurement of attenuation coefficients of weakly scattering media using optical coherence tomography," *Opt. Express* **12**(19), 4353–4365 (2004).
16. R. Leitgeb, C. Hitzenberger, and A. Fercher, "Performance of Fourier domain vs. time domain optical coherence tomography," *Opt. Express* **11**(8), 889–894 (2003).
17. N. Nassif et al., "In vivo high-resolution video-rate spectral-domain optical coherence tomography of the human retina and optic nerve," *Opt. Express* **12**(3), 367–376 (2004).
18. V. M. Kodach et al., "Determination of the scattering anisotropy with optical coherence tomography," *Opt. Express* **19**(7), 6131–6140 (2011).
19. N. Bosschaart et al., "Measurements of wavelength dependent scattering and backscattering coefficients by low-coherence spectroscopy," *J. Biomed. Opt.* **16**(3), 030503 (2011).
20. H. R. G. W. Verstraete et al., "Towards model-based adaptive optics optical coherence tomography," *Opt. Express* **22**(26), 32406–32418 (2014).
21. B. Cense et al., "Ultrahigh-resolution high-speed retinal imaging using spectral-domain optical coherence tomography," *Opt. Express* **12**(11), 2435–2447 (2004).
22. S. L. Jacques et al., "Measuring tissue optical properties in vivo using reflectance-mode confocal microscopy and OCT," *Proc. SPIE* **6864**, 68640B (2008).
23. H. C. van der Hulst, *Light Scattering by Small Particles*, Dover Publications, New York (1957).
24. L. Tsang et al., *Scattering of Electromagnetic Waves, Numerical Simulations*, John Wiley & Sons, Inc., Hoboken, New Jersey (2001).
25. G. M. Hale and M. R. Querry, "Optical constants of water in the 200-nm to 200-$\mu$m wavelength region," *Appl. Opt.* **12**(3), 555–563 (1973).
26. G. Singh and L. Song, "Influence of sodium dodecyl sulfate on colloidal fouling potential during ultrafiltration," *Colloids Surf. A* **281**, 138–146 (2006).
27. T. R. Hillman et al., "Correlation of static speckle with sample properties in optical coherence tomography," *Opt. Lett.* **31**(2), 190 (2006).
28. J. W. Goodman, *Speckle Phenomena in Optics: Theory and Applications*, Roberts and Company Publishers, Greenwood Village, Colorado (2007).
29. D. Levitz et al., "Quantitative characterization of developing collagen gels using optical coherence tomography," *J. Biomed. Opt.* **15**(2), 026019 (2010).
30. J. J. ten Bosch, "Pascal program to perform Mie calculations," *Opt. Eng.* **32**(7), 1691–1695 (1993).
31. I. H. Malitson, "Interspecimen comparison of the refractive index of fused silica," *J. Opt. Soc. Am.* **55**(10), 1205 (1965).
32. K. F. Palmer and D. Williams, "Optical properties of water in the near infrared," *J. Opt. Soc. Am.* **64**(8), 1107 (1974).
33. R. Wessels et al., "Learning curve and inter-observer variance in quantification of the optical coherence tomography attenuation coefficient," *J. Biomed. Opt.* **20**(12), 121313 (2015).
34. K. A. Vermeer et al., "Depth-resolved model-based reconstruction of attenuation coefficients in optical coherence tomography," *Biomed. Opt. Express* **5**(1), 322–337 (2014).
35. M. T. J. Bus et al., "Volumetric in vivo visualization of upper urinary tract tumors using optical coherence tomography: a pilot study," *J. Urol.* **190**(6), 2236–2342 (2013).
36. K. Barwari et al., "Advanced diagnostics in renal mass using optical coherence tomography: a preliminary report," *J. Endourol.* **25**(2), 311–315 (2011).
37. N. Bosschaart et al., "A literature review and novel theoretical approach on the optical properties of whole blood," *Lasers Med. Sci.* **29**(2), 453–479 (2014).
38. U. A. Gamm et al., "Measurement of tissue scattering properties using multi-diameter single fiber reflectance spectroscopy: in silico sensitivity analysis," *Biomed. Opt. Express* **2**(11), 3150 (2011).
39. J. M. Schmitt and G. Kumar, "Turbulent nature of refractive-index variations in biological tissue," *Opt. Lett.* **21**(16), 1310–1312 (1996).
40. J. M. Schmitt and G. Kumar, "Optical scattering properties of soft tissue: a discrete particle model," *Appl. Opt.* **37**(13), 2788–2797 (1998).
41. J. M. Steinke and A. P. Shepherd, "Comparison of Mie theory and the light scattering of red blood cells," *Appl. Opt.* **27**(19), 4027–4033 (1988).
42. D. J. Faber et al., "Toward assessment of blood oxygen saturation by spectroscopic optical coherence tomography," *Opt. Lett.* **30**(9), 1015–1017 (2005).
43. D. J. Faber and T. G. van Leeuwen, "Are quantitative attenuation measurements of blood by optical coherence tomography feasible?" *Opt. Lett.* **34**(9), 1435–1437 (2009).

**Mitra Almasian** is a PhD candidate in the Biomedical Engineering and Physics Department of the Academic Medical Center (AMC), University of Amsterdam, Amsterdam, The Netherlands. Her research is focused on optical coherence tomography. After an interdisciplinary bachelor with a major in chemistry, she received her master's degree in physical sciences from the University of Amsterdam in 2012.

**Nienke Bosschaart** is an assistant professor at the Biomedical Photonic Imaging Group (BMPI) of the MIRA Institute at the University of Twente, Enschede, The Netherlands. She received her PhD at the AMC of the University of Amsterdam in 2012. Her research interests are the noninvasive quantification of tissue (optical) properties for medical diagnostics, in particular using low-coherence spectroscopy and spectroscopic optical coherence tomography.

**Ton G. van Leeuwen** is full professor in biomedical physics and in 2008 was appointed as head of the Biomedical Engineering and Physics Department at the Academic Medical Center of the University of Amsterdam. His current research focuses on the physics of the interaction of light with tissue, and using that knowledge for the development, introduction, and clinical evaluation of newly developed optical imaging techniques for gathering quantitative functional and molecular information of tissue.

**Dirk J. Faber** is an assistant professor (Universitair Docent) of biomedical optics at the Department of Biomedical Engineering and Physics of the AMC, University of Amsterdam. He studied applied physics at the University of Twente in 2000 and graduated in "Functional Optical Coherence Tomography" at AMC in 2005. His research interests are the physics of light–tissue interaction with specific application to cancer diagnosis.